Seismic Monitoring and Geomorphic Impacts of the Catastrophic 2018 Baige Landslide Hazard Cascades in the Tibetan Plateau

Zhen Zhang, Yen Joe Tan, Fabian Walter, Siming He, Malgorzata Chmiel, Jinrong Su

▶ **To cite this version:**

Zhen Zhang, Yen Joe Tan, Fabian Walter, Siming He, Malgorzata Chmiel, et al.. Seismic Monitoring and Geomorphic Impacts of the Catastrophic 2018 Baige Landslide Hazard Cascades in the Tibetan Plateau. Journal of Geophysical Research: Earth Surface, 2024, 129 (2), 10.1029/2023jf007363 . hal-04488341

HAL Id: hal-04488341
https://hal.science/hal-04488341

Submitted on 4 Mar 2024

HAL is a multi-disciplinary open access archive for the deposit and dissemination of scientific research documents, whether they are published or not. The documents may come from teaching and research institutions in France or abroad, or from public or private research centers.

L'archive ouverte pluridisciplinaire **HAL**, est destinée au dépôt et à la diffusion de documents scientifiques de niveau recherche, publiés ou non, émanant des établissements d'enseignement et de recherche français ou étrangers, des laboratoires publics ou privés.

Check for updates

JGR Earth Surface

RESEARCH ARTICLE
10.1029/2023JF007363

Seismic Monitoring and Geomorphic Impacts of the Catastrophic 2018 Baige Landslide Hazard Cascades in the Tibetan Plateau

Zhen Zhang[1,2], Yen Joe Tan[1], Fabian Walter[3], Siming He[2], Małgorzata Chmiel[3,4], and Jinrong Su[5]

[1]Earth and Environmental Sciences Programme, Faculty of Science, The Chinese University of Hong Kong, Hong Kong S.A.R., China, [2]Institute of Mountain Hazards and Environment, Chinese Academy of Sciences, Chengdu, China, [3]Swiss Federal Institute for Forest, Snow and Landscape Research WSL, Birmensdorf, Switzerland, [4]Géoazur, Observatoire de la Côte d'Azur, Université Côte d'Azur, CNRS, IRD, Sophia-Antipolis, France, [5]Earthquake Monitoring Center, Sichuan Earthquake Administration, Chengdu, China

Key Points:

- Catastrophic outburst floods were surprisingly quiet with peak seismic energy preceding peak discharge due to changes in channel stability
- Various dam breach processes can be well-characterized seismically, which can constrain numerical modeling and provide earlier warning
- These hazard cascades drastically increased sediment fluxes ≥670 km downstream for years and reduced hydropower plant capacity

Supporting Information:

Supporting Information may be found in the online version of this article.

Correspondence to:

Y. J. Tan,
yjtan@cuhk.edu.hk

Citation:

Zhang, Z., Tan, Y. J., Walter, F., He, S., Chmiel, M., & Su, J. (2024). Seismic monitoring and geomorphic impacts of the catastrophic 2018 Baige landslide hazard cascades in the Tibetan plateau. *Journal of Geophysical Research: Earth Surface*, *129*, e2023JF007363. https://doi.org/10.1029/2023JF007363

Received 28 JUL 2023
Accepted 19 JAN 2024

© 2024. The Authors.
This is an open access article under the terms of the Creative Commons Attribution License, which permits use, distribution and reproduction in any medium, provided the original work is properly cited.

Abstract Surface hazards can form hazard cascades which expand their reach. However, our understanding of their complex dynamics and ability to mitigate their impacts remain limited. In 2018, two landslides dammed the Jinsha River in the Tibetan plateau and formed landslide-dammed lakes. Subsequent dam breaches prompted the evacuation of >120,000 people. An early warning system for floods using a regional seismic network has been proposed on the basis of catastrophic floods having been detected ~100 km away, with seismic energy proportional to discharge. Surprisingly, we find that this catastrophic outburst flood was undetectable beyond a few kilometers, with peak seismic energy preceding peak discharge. We propose that river channel stability also controls seismic energy generation and should be considered for accurate monitoring of catastrophic floods. In contrast, we find that the various processes during dam breach can be well-characterized seismically further away and provide warning ~60 min before discharge exceeds monsoon flood levels. We also show that numerical modeling of dam breaches which typically lacks in situ measurements can benefit from incorporating seismic data as constraints. Finally, we show that this event drastically increased sediment fluxes ~670 km downstream for years and may significantly reduce the capacity of hydropower plants. Our results reveal ways to improve early warning of catastrophic outburst floods and the need to consider surface hazards' long-term impact when managing infrastructure in mountainous regions.

Plain Language Summary Mountainous regions are prone to surface hazards such as landslides and floods. However, our understanding of how these events evolve and interact is limited. In 2018, two landslides blocked a river in Tibet and created landslide-dammed lakes. Subsequently, the dam broke and the resulting outburst floods severely damaged downstream infrastructure and led to the evacuation of >120,000 people. In contrast to what previous studies suggest, we find that this catastrophic outburst flood was undetectable beyond a few kilometers, with peak seismic energy preceding peak discharge. We propose that river channel stability also controls seismic energy generation and should be considered for accurate monitoring of catastrophic floods. Conversely, the dam breakage could be detected seismically further away and provide warning ~60 min before discharge exceeded monsoon flood levels. Finally, we show that this event drastically increased sediment amounts downstream for years and may reduce the capacity of hydropower plants. Our results reveal ways to improve seismic monitoring and early warning of catastrophic floods and the need to consider the long-term impact of surface hazards when managing downstream infrastructure.

1. Introduction

Approximately 12% of the world's population (~720 million people) live in mountainous regions (Price, 2013), which are susceptible to surface hazards such as landslides (Gariano & Guzzetti, 2016), avalanches (Schweizer et al., 2003; Shugar et al., 2021), and debris flows (Iverson et al., 2011). Some events can further form hazard cascades which expand their reach and impact (Shugar et al., 2021). For example, the 2000 Yigong landslide in the Tibetan plateau blocked the Yigong Zangpo River (Tibet) and formed a ~2×10^9 m^3 landslide-dammed lake (LDL) (Delaney & Evans, 2015; Shang et al., 2003). The landslide dam subsequently breached 62 days later and generated catastrophic outburst floods that impacted as far downstream as India and Bangladesh (Delaney & Evans, 2015; Shang et al., 2003). As a warming climate exacerbates such surface hazards (Jaedicke et al., 2008)

21699011, 2024, 2, Downloaded from https://agupubs.onlinelibrary.wiley.com/doi/10.1029/2023JF007363 by Université Côte d'Azur, Wiley Online Library on [04/03/2024]. See the Terms and Conditions (https://onlinelibrary.wiley.com/terms-and-conditions) on Wiley Online Library for rules of use; OA articles are governed by the applicable Creative Commons License

and population growth and infrastructure development contribute to increasing exposure (Ozturk et al., 2022), our ability to manage these surface hazards is critical for sustainable development in mountainous regions.

Surface hazard management would benefit from developing early warning systems and understanding the complex physical mechanisms and long-term impact of these hazards. Typically, the monitoring of these surface hazards relies on satellite remote sensing (Irons et al., 2012; Tralli et al., 2005; Wasowski & Bovenga, 2014) and in situ sensors (Arattano & Marchi, 2008; McCoy et al., 2010). While satellite remote sensing can track these events at meter-scale resolution over most of our planet, typical satellite revisit times of the order of days preclude real-time monitoring and early warning. In comparison, in situ sensors such as force plates and flow stage sensors used to detect and monitor floods (Habersack et al., 2017; McArdell et al., 2007) can provide high temporal resolution data but have much smaller spatial coverage and can be challenging to install and maintain (Le Guern et al., 2020; Vericat et al., 2006). In addition, while numerical models can be used to simulate certain surface hazards (Khrapov et al., 2013), they require sufficient understanding of the underlying physical mechanisms and well-constrained physical parameters as inputs (Anees et al., 2016; Yavari-Ramshe & Ataie-Ashtiani, 2016).

In recent years, seismometers have been shown to be capable of tracking various surface hazards in real-time at remote distances (Chmiel et al., 2022; Dietze et al., 2022; Ekström & Stark, 2013; Zhang et al., 2021), and are a promising alternative tool to quantify the dynamics and evolution of these processes. Early warning systems for catastrophic floods using regional seismic networks have also been proposed based on these events having been detected ∼100 km away (Cook et al., 2021; Maurer et al., 2020). However, while models explaining how certain surface processes radiate seismic energy have been proposed, our understanding of extreme events remains limited and incomplete. For example, while existing models propose that floods' seismic signals are produced by the impacts of moving bedload particles (Tsai et al., 2012) and the energy transmitted to the river bed and banks by turbulent flow (Gimbert et al., 2014), whether seismic energy always increases with discharge as these models predict and whether there are other important physical processes/factors that also affect the generation of catastrophic floods' seismic signals (Maurer et al., 2020) are still open questions. In addition, no model has yet been proposed to explain seismic signals generated during dam breaches. This makes it difficult to ascertain the general effectiveness of currently proposed early warning systems (Cook et al., 2021; Maurer et al., 2020).

Since surface hazards can mobilize coarse sediments as well as erode and reorganize river channels (Hovius et al., 1997; Schaller et al., 2001), they are also well-known to impact geomorphic evolution (Cook et al., 2018; Schaller et al., 2001; Tramblay et al., 2020). However, previous studies have typically focused on the short-term impact on geomorphic systems by quantifying terrain changes immediately before and after these events (Cook et al., 2018; Shugar et al., 2021). Therefore, the lack of longer-term in situ observations (Garcia-Castellanos & O'Connor, 2018; Shugar et al., 2021) means that our understanding of the lasting impact of such hazards on geomorphic systems, which might also affect downstream hydropower plants and reservoirs (Hewawasam, 2010; Zhang et al., 2015), remains limited.

On 10 October and 3 November 2018, two successive landslides in the Tibetan plateau (Figure 1a; Zhang, He, et al., 2019; Zhang, Xiao, et al., 2019; Zhong et al., 2020; Fan, Yang, et al., 2020; Gao et al., 2021; Chen et al., 2021) blocked the Jinsha River, which is the upper course of the Yangtze River, and created two LDLs. The subsequent dam breaches resulted in massive outburst floods that caused the immediate evacuation of >120,000 people (NDRCC, 2018b, 2018a) and severe damage/destruction of 27,000 houses, 8 bridges, 4 hydropower plants, and 33,000 ha of farmland up to 670 km downstream (Chen et al., 2021; Fan, Yang, et al., 2020; Gao et al., 2021; Zhang, Xiao, et al., 2019; Zhong et al., 2020). The second landslide lake outburst flood (LLOF), with peak discharge of ∼31,000 m^3/s and volume of 5.8×10^8 m^3 (Chen et al., 2021; Fan, Yang, et al., 2020; Gao et al., 2021; Zhong et al., 2020), is the largest recorded LLOF of the 21st century to date and provides a unique opportunity to understand such hazard cascades. Here, we integrate seismic observations with hydrological data, videos/photographs, satellite observations, and numerical modeling to study the detailed seismic signatures, evolution, and impact of the hazard cascades. Our results reveal ways to improve seismic monitoring and early warning of catastrophic floods and the potential long-term impact of surface hazards on river systems and downstream hydropower plants.

2. Study Site and Case

At 22:05 China Standard Time (CST) on 10 October 2018, a landslide initiated in Baige at about 3,700 m asl and transported 2.5×10^7 m^3 of sediments into the Jinsha River at about 2,870 m asl (Figure 1a; Chen et al., 2021;

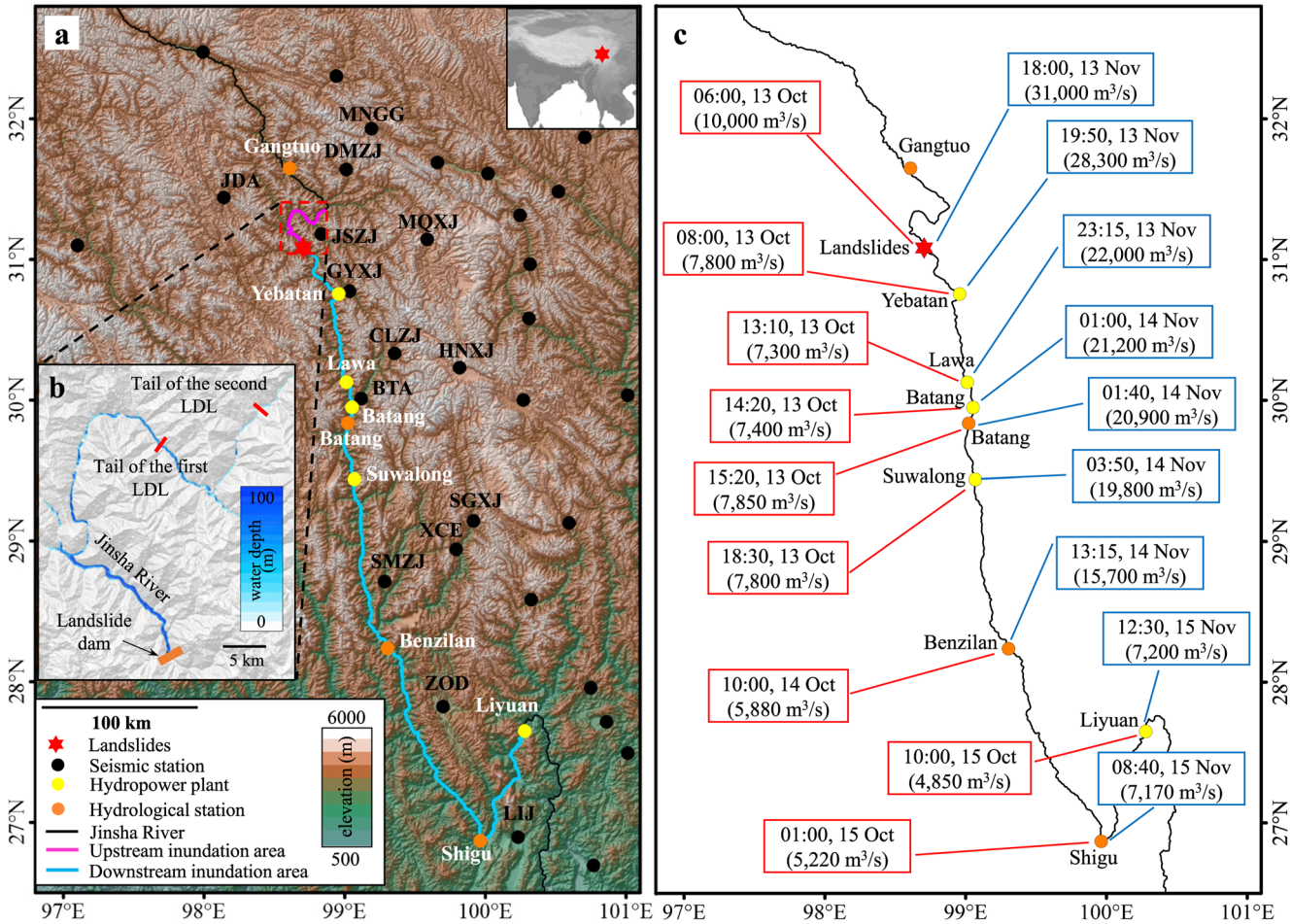

Figure 1. Landslide-dammed lakes and outburst floods. (a) Study area with the locations of hydropower plants, hydrological stations, and seismic stations. The names of the seismic stations used in our analyses are marked. (b) Inundation areas of the landslide-dammed lakes. (c) Timings and amplitudes of peak discharges of the first (red box) and second (blue box) outburst floods recorded at different hydrological stations and hydropower plants. Digital elevation model source: Advanced Spaceborne Thermal Emission and Reflection Radiometer.

Fan, Yang, et al., 2020; Gao et al., 2021; Zhong et al., 2020). This ~61 m high landslide dam created a large LDL that inundated terrain up to ~45 km upstream (Figure 1b). The LDL naturally breached the west side of the landslide dam at 17:15 CST on 12 October. With the dam breach, the discharge rapidly increased to a maximum of 10,000 m^3/s at 06:00 CST on 13 October before gradually decreasing back to the same level as the flow upstream feeding the LDL at 22:00 CST on 13 October.

Three weeks later at 17:40 CST on 3 November, a second landslide in Baige transported an additional 8.7×10^6 m^3 of materials into the Jinsha River. This smaller landslide deposited atop the residual dam from the first landslide and created a higher dam that was at least 96 m high that inundated terrain up to ~70 km upstream (Figure 1b; Chen et al., 2021; Fan, Yang, et al., 2020; Gao et al., 2021; Zhong et al., 2020). To mitigate the potential damage from an unexpected outburst flood, the Yangtze River Flood Control and Drought Relief Headquarters dug a ~15 m deep drainage trench on the west side of the dam (Zhong et al., 2020). Water started flowing into the drainage trench at 04:45 CST on 12 November, which initiated the erosion of the top and downstream face and subsequent sediment collapse at the breach side slope of the landslide dam (Figure S2 in Supporting Information S1). The dam breach was well-recorded by a dense network of seismometers operated by the China Earthquake Administration (Figure 1a).

21699011, 2024, 2, Downloaded from https://agupubs.onlinelibrary.wiley.com/doi/10.1029/2023JF007363 by Université Côte d'Azur, Wiley Online Library on [04/03/2024]. See the Terms and Conditions (https://onlinelibrary.wiley.com/terms-and-conditions) on Wiley Online Library for rules of use; OA articles are governed by the applicable Creative Commons License

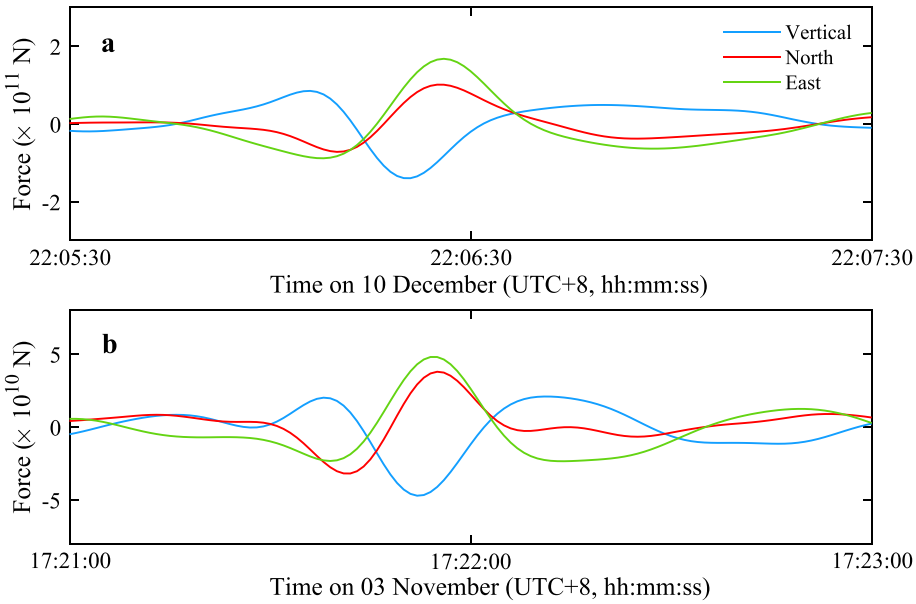

Figure 2. Landslide force vector during runout. (a) and (b) are the first and the second landslides' forces inverted from seismic signals, respectively.

3. Materials and Methods

3.1. Seismic Data Processing

All stations used in this study (Figure 1a) are operated by the China Earthquake Administration and equipped with a 3-component broadband seismometer with a sampling rate of 100 Hz. Due to the rapid attenuation of high-frequency seismic energy, >5 Hz seismic signals generated by dam breach and flood were not visible above the background noise level at these stations. Hence, we focus on 0.5–5 Hz seismic signals for our study. After removing the instrumental response, using Welch's method, we calculate the power spectral density (PSD) of seismic signals with time window of 200 s. We then estimated the signal's peak frequencies for the 200-s moving time windows, excluding time windows that included seismic signals from local earthquakes.

3.2. Landslide Force Vector Inversion

Acceleration/deceleration of the two landslides, accompanying landslide initiation, movement, and deposition, generates long-period seismic signals that attenuate slowly and are less sensitive to heterogeneities; hence, they can be recorded by seismic stations several hundred kilometers away (Ekström & Stark, 2013; Zhang, He, et al., 2019). The measured seismic signals contain information about the source and its propagation path. In the case where the landslide path is much shorter than the landslide-to-station distance, the single-point force well approximates the force exerted by the landslide on the hillslope during run-out (Zhang, He, et al., 2019). We treat the Green's function as the effect of the seismic wave path through the Earth and calculate it using the 1-D ak135 Earth velocity and an elastic attenuation model based on the matrix propagation method (Wang, 1999). Next, according to the damped least squares approach, we use the long-period (from 20 to 80 s for the first landslide and from 20 to 60 s for the second landslide) seismic signals recorded by 12 seismic stations within 200 km to invert for the force vector exerted by the landslide on the slope (Figure 2). Information about these seismic stations is shown in Table S1 in Supporting Information S1.

3.3. Dam Breach Modeling

We model the breach process of the second landslide dam due to overtopping using the DLBreach software (Figure S1 in Supporting Information S1). This landslide dam breach is simplified as a two-way breach of a homogeneous non-cohesive dam by overtopping (Wu, 2013, 2016). The simulation includes hydrodynamics, sediment erosion, and breach enlargement processes. For the hydrodynamics, the Weir equation is used to calculate the breach flow during the intensive breaching or erosion stage (Singh & Snorrason, 1984; Wang &

21699011, 2024, 2, Downloaded from https://agupubs.onlinelibrary.wiley.com/doi/10.1029/2023JF007363 by Université Côte d'Azur, Wiley Online Library on [04/03/2024]. See the Terms and Conditions (https://onlinelibrary.wiley.com/terms-and-conditions) on Wiley Online Library for rules of use; OA articles are governed by the applicable Creative Commons License

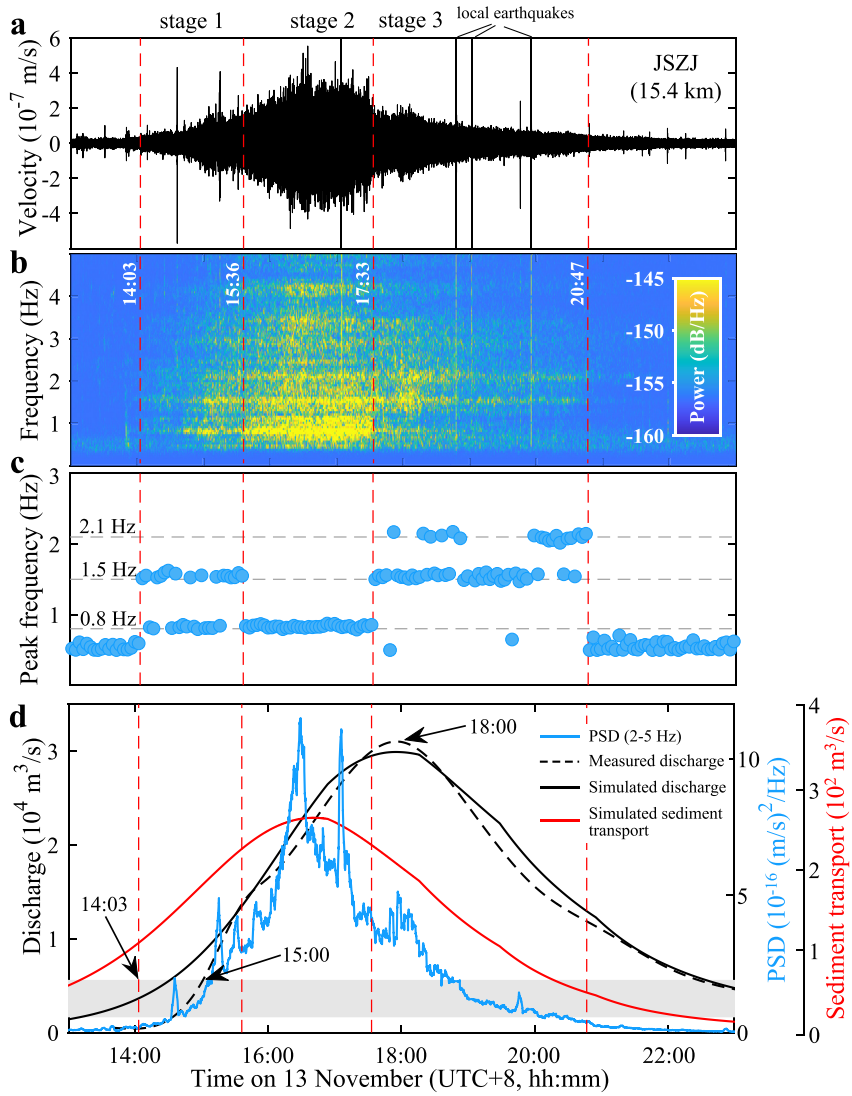

Figure 3. Seismic signals and discharge during the second landslide dam breach. (a) and (b) 0.5–5 Hz seismic signals recorded at station JSZJ and its spectrogram. (c) Peak frequencies calculated for 200 s moving time windows. (d) Measured and simulated discharge at the breach, simulated sediment transport, and power spectral density (PSD) of 2–5 Hz seismic signals. The PSD is smoothed with a 200 s moving time window. Gray bar indicates the range of annual maximum discharges (1,620–5,610 m^3/s) recorded at the Batang hydrological station (Figure 1a) from 1963 to 2021, excluding 2018 and years when data are not available. Timings of some key events are marked.

Bowles, 2006), while the Keulegan equation is used to estimate the breach flow during the general breach or inlet evolution stage (Wu, 2013, 2016). For the sediment erosion, a non-equilibrium total-load transport model is used for the erosion of the second landslide dam (Armanini & Di Silvio, 1988; Sánchez & Wu, 2011). For breach development, the simulation was run to calculate the volumetric bed change using time steps of 0.2 s. The volume change can then be converted to bed change and width change along the breach cross-section, which involves the sediment collapse/mass failure of breach side slopes (Figure S1 in Supporting Information S1). Since there are already sufficient field surveys, laboratory experiments, and numerical simulations on this dam breach (e.g., Chen et al., 2020; Zhong et al., 2020), the key input parameters used to simulate the dam breach are well documented and are listed in Table S2 in Supporting Information S1. For the less well-constrained input parameters such as porosity and adaption coefficient, while changes in these parameters affect the temporal evolution of discharge and sediment transport, the peak sediment transport always preceded peak in measured discharge

21699011, 2024, 2, Downloaded from https://agupubs.onlinelibrary.wiley.com/doi/10.1029/2023JF007363 by Université Côte d'Azur, Wiley Online Library on [04/03/2024]. See the Terms and Conditions (https://onlinelibrary.wiley.com/terms-and-conditions) on Wiley Online Library for rules of use; OA articles are governed by the applicable Creative Commons License

by hours (Figure S2 in Supporting Information S1). Therefore, our main conclusion is robust and our preferred model is the one where the simulated and measured discharges are aligned (Figure 3d).

3.4. Measured Discharge and Seismic Signals of LLOF

Although seismic stations GYXJ and BTA are located close to hydrological stations that can provide measured discharge data (Figure 1a), the nearest points of the river channel to stations GYXJ and BTA are still ∼1.5 and 7.8 km upstream of the Yebatan hydropower plant and Batang hydropower plant, respectively. We thus calculate the arrival time difference of the flood passing through the hydropower plants and the nearest point of the river channel to the seismic stations using the average flow propagation speed.

Based on the hydrological measurements, we know that it took 120 and 110 min (Figure 1c) for the peak flows of the two floods to travel ∼54 km from the breach to the Yebatan hydropower plant. Hence, the average flow propagation speeds of the two flood peaks passing through the Yebatan plant are 7.5 and 8.2 m/s, respectively. Therefore, the arrival time differences between the two floods passing by seismic station GYXJ and the Yebatan hydropower plant are 200 and 180 s, respectively. In comparison, it took 70 and 105 min (Figure 1c) for the peak flows of the two floods to travel ∼25 km from the Lawa to the Batang hydropower plant. Hence, the average flow propagation speeds of the two flood peaks passing through the Batang station are 6.0 and 4.0 m/s, respectively. Therefore, the arrival time differences between the two floods passing by seismic station BTA and the Batang hydropower plant are 1,300 and 1,950 s. The estimated arrival time differences are then used to align the timings of the recorded discharges and seismic signals. Finally, we assume the flow discharges recorded by the Yebatan and Batang hydropower plants as the flow discharges when the outburst floods passed by stations GYXJ and BTA, respectively.

3.5. Sediment Flux Data and Water Surface Width Changes

Measured sediment flux data at the Batang and Shigu hydrological stations were extracted from the Chinese Hydrological Data Yearbook published by the Ministry of Water Resources, China. Note that, like most rivers in the world, the bedload flux in the Jinsha River has not been systematically monitored. Therefore, we only focus on the suspended sediment flux.

The water surface width changes were estimated from Sentinel-2 RGB images which have 10 m resolution. In order to reduce the effect from changes in discharge and vegetation, we selected images from the same month (December) each year from 2015 to 2021, which had similar discharges (Table S3 in Supporting Information S1), to estimate the river water surface widths. We confirm that data from other winter months show similar trends. We focus on the region from 30 km upstream to 100 km downstream of the landslide dam, which is covered by two tiles. The date of the selected images and the associated discharges are listed in Table S3 in Supporting Information S1. For each image, we manually delineate the margins of the river water surface and then smooth the data with a 1-km moving window. Finally, we take the river water surface width in December 2017 as the reference to calculate annual water surface width changes.

4. Results

4.1. Landslide Dynamics

The shape of the force-time functions of the two landslides are similar, suggesting that the two landslides have similar travel processes (Figure 2). The failure of the material at about 3,700 m elevation initiated at 22:05:46 October 10 (Beijing time, UTC + 8; all subsequent time are given in Beijing time) for the first event and at 17:21:30 November 3 for the second event, and moved downward rapidly, generating an upward force. As the material on the hillslope is eroded and entrained, the volume of the two landslides gradually increased to approximately 24 million and 8.7 million m^3 (Chen et al., 2021; Fan, Yang, et al., 2020; Gao et al., 2021) before entering the Jinsha river at 22:06:21 October 10 (Zhang, He, et al., 2019) and 17:21:53 November 3 respectively, generating the downward subvertical forces with a northeastward component, consistent with the boundary of the impact area. As the first landslide rushed into the river, a landslide dam with a length of ∼1,200 m, width of 143 m, and minimum height of ∼51 m, formed (Chen et al., 2021; Gao et al., 2021). Although the volume of the second landslide is smaller, this event blocked the natural drainage channel of the first dam and formed a larger dam with minimum height of ∼96 m (Chen et al., 2021; Gao et al., 2021; Zhong et al., 2020).

21699011, 2024, 2, Downloaded from https://agupubs.onlinelibrary.wiley.com/doi/10.1029/2023JF007363 by Université Côte d'Azur, Wiley Online Library on [04/03/2024]. See the Terms and Conditions (https://onlinelibrary.wiley.com/terms-and-conditions) on Wiley Online Library for rules of use; OA articles are governed by the applicable Creative Commons License

21699011, 2024, 2, Downloaded from https://agupubs.onlinelibrary.wiley.com/doi/10.1029/2023JF007363 by Université Côte d'Azur, Wiley Online Library on [04/03/2024]. See the Terms and Conditions (https://onlinelibrary.wiley.com/terms-and-conditions) on Wiley Online Library for rules of use; OA articles are governed by the applicable Creative Commons License

4.2. Evolution of Dam Breaches

While some dam breaches have been recorded seismically (Feng, 2009; Yang et al., 2022), how the evolution of various dam breach processes can be inferred from their seismic signals remains underexplored. The first dam breach event generated 0.5–5 Hz seismic energy that was clearly recorded by station JSZJ at ∼15 km away starting 00:45 CST on 13 Oct and lasting for ∼6 hr before the station failed due to unknown reasons (Figure S3 in Supporting Information S1). The seismic signal's peak frequencies are mainly at 0.8 and 2.1 Hz. Similarly, the second dam breach event generated seismic energy that was clearly recorded starting 14:03 CST on 13 Nov and lasting for ∼6.5 hr (Figure 3). However, the peak seismic frequencies varied between 0.8, 1.5, and 2.1 Hz at different time periods.

We interpret that the three peak frequencies were generated by (a) the collapse of breach side slope which is similar to landslides that can generate low-frequency (<1 Hz) seismic signals (Ekström & Stark, 2013), (b) turbulent flow which tends to radiate high-frequency (>1 Hz) seismic signals (Gimbert et al., 2014), and (c) bedload transport which tends to radiate even higher-frequency seismic energy than turbulent flow (Gimbert et al., 2014; Tsai et al., 2012). The 1.5 Hz turbulent flow seismic energy is apparent at certain stages during the second dam breach because unlike the first dam which only contained easily erodible sediments, the second dam contained huge boulders that are difficult to transport (Chen et al., 2021; Fan, Yang, et al., 2020) and can radiate stronger turbulent seismic energy through interaction with water flow.

The variability of peak frequency content divides the second dam breach process into three distinct stages (Figure 3). The first stage, which lasted ∼1.5 hr, contains peak frequencies of 0.8 and 1.5 Hz, which suggests that both slope collapse and turbulent flow are the dominant processes emitting seismic energy. Subsequently, as the discharge increased, the seismic signal became dominated primarily by the 0.8 Hz peak frequency over the next 2 hr. This is consistent with field observations (Zhong et al., 2020) of large numbers of materials on the breach side walls collapsing due to increasing trench erosion which resulted in rapid trench enlargement and maximum seismic energy during this time period (Figure 3). Eventually, the 0.8 Hz seismic energy dropped out, which suggests that the trench enlargement process slowed down and eventually stopped. At this point, the discharge reached a peak of ∼31,000 m^3/s (Figure 3c) which far exceeds the 10,000-year return period discharge of ∼11,500 m^3/s at the site (Zhang, Xiao, et al., 2019) and is more than 10 times larger than previously reported peak discharges of lake outburst floods (LOFs) that were recorded by regional seismic networks, such as the ∼2,500 and 2,400 m^3/s for the 1994 Lugge Tsho (Maurer et al., 2020) and the 2016 Gongbatongshacuo LOFs (Cook et al., 2018), respectively. As the discharge reached its maximum at 18:00 CST on 13 October, there was a second smaller peak in seismic energy (Figure 3c) with the seismic signal dominated by peak frequencies of 1.5 and 2.1 Hz, which reflect turbulent flow and bedload transport. This is consistent with existing fluvial seismic models (Gimbert et al., 2014; Tsai et al., 2012) which showed that both the bedload sediment transport and the interaction between the turbulent flow and bed/bank generate seismic signals and they correlate with discharge (Bakker et al., 2020).

Our numerical modeling of the dam breach shows that the simulated sediment flux's temporal evolution correlates with the PSD of the recorded 2–5 Hz seismic signal (Figure 3d). This supports our interpretation that the highest peak frequency (2.1 Hz) seismic signals are dominated by bedload sediment transport. This also suggests that seismic recordings can potentially improve numerical modeling of dam breaches by constraining sediment flux's temporal evolution, since monitoring of sediment flux is a significant challenge even for well-documented dam breaches due to their catastrophic nature (Wahl, 2004). In addition, due to the unpredictability of dam breaches, monitoring the temporal evolution of drainage trenches and discharge during dam breaches is also a challenge. Since seismic data contain information on multiple physical processes of dam breaches, such as the drainage trench's evolution and discharge, the numerical modeling of dam breaches can benefit from incorporating seismic data as constraints. Finally, we find that the dam breach seismic signal at station JSZJ is clearly observed at 14:03 which is ∼4 hr before the time of peak discharge and ∼60 min before the resulting LLOF's measured discharge exceeds the typical monsoon flood discharge level (Figure 3). Furthermore, the dam breach seismic signals are clearly detected outside the anthropogenic noise frequency band by stations up to ∼66 km away (Figure S4 in Supporting Information S1).

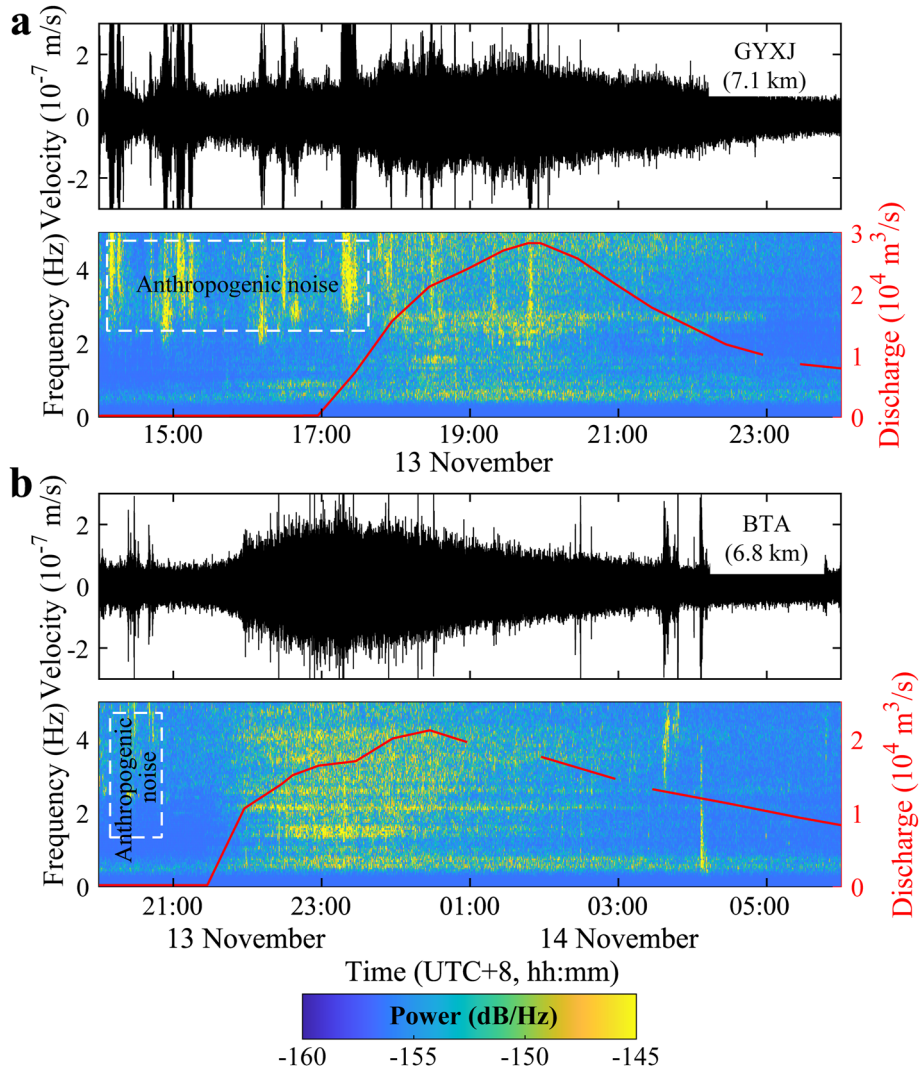

Figure 4. Discharge versus the seismic signals generated by the second outburst flood. (a) and (b) 0.5–5 Hz seismic signals during the second outburst flood recorded at stations GYXJ and BTA, their spectrograms, and measured discharge of the flood. The distances from the stations to the river channel are listed. White dashed boxes mark the inferred anthropogenic noise.

4.3. Evolution of Outburst Floods

As the first LLOF traveled down to the Jinsha River, its peak flow decreased from 7,850 m^3/s at Batang hydrological station at 15:20 CST on 13 November to 5,880 m^3/s at Benzilan hydrological station at 10:00 CST on 14 October to 5,220 m^3/s at Shigu hydrological station at 01:00 CST on 15 October (Figure 1c). Finally, the peak flow decreased to 4,850 m^3/s at 10:00 CST on 15 October when it entered the Liyuan hydropower plant. As the second LLOF traveled down to the Jinsha River, its peak flow decreased to 20,900 m^3/s at 1:00 CST on 14 Nov, 15,700 m^3/s at 13:15 CST on 14 Nov, and 7,170 m^3/s at 8:40 CST on 15 Nov, according to discharge measurements at the Batang, Benzilan, and Shigu hydrological stations ~190, 380, and 560 km downstream of the landslide dam, respectively (Figure 1c). Finally, the peak flow decreased to 7,200 m^3/s at 12:30 on 15 November when entering the Liyuan hydropower plant ~670 km downstream of the landslide dam.

As the second LLOF traveled downstream and passed through four hydropower plants, its peak discharge along most of this flow path (Figure 1c) was significantly larger than the catastrophic 2021 Chamoli, India (Shugar et al., 2021–14,200 m^3/s) flood that was detected by regional seismic stations ~100 km away. However, seismic signals of this LLOF were only visible at two stations within 10 km (Figure 4) and not visible at stations beyond

21699011, 2024, 2, Downloaded from https://agupubs.onlinelibrary.wiley.com/doi/10.1029/2023JF007363 by Université Côte d'Azur, Wiley Online Library on [04/03/2024]. See the Terms and Conditions (https://onlinelibrary.wiley.com/terms-and-conditions) on Wiley Online Library for rules of use; OA articles are governed by the applicable Creative Commons License

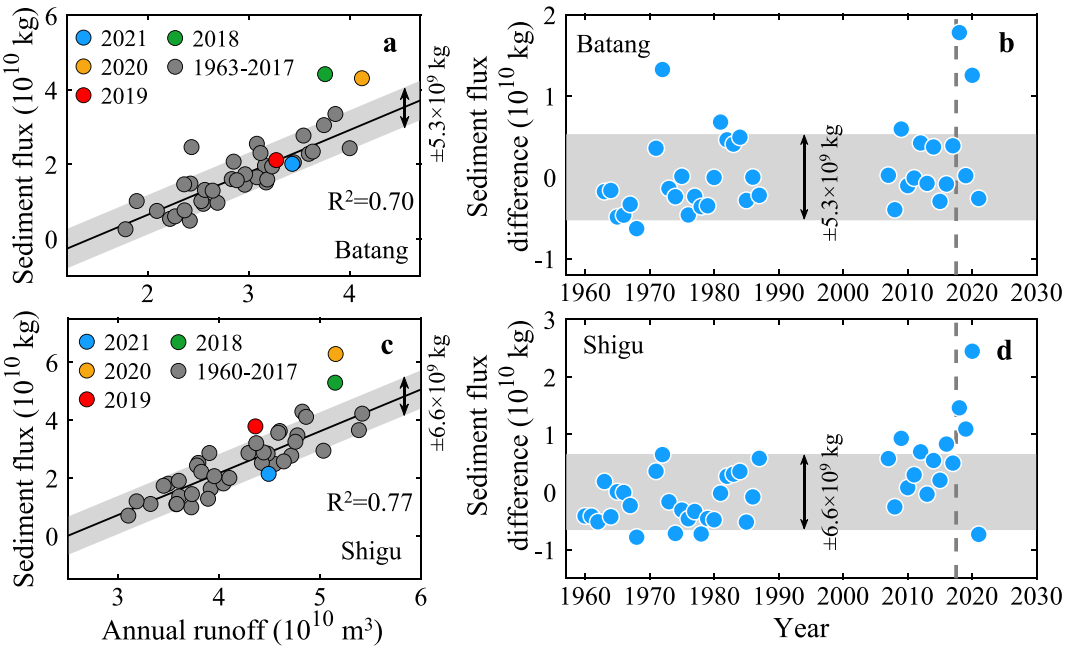

Figure 5. Measured sediment flux at hydrological stations. (a) and (c) Measured annual runoff versus sediment flux at the Batang and Shigu hydrological stations ~190 and 560 km downstream from the landslides. Black lines indicate the linear fit using measurements from 1963 to 2017 in Batang and from 1960 to 2017 in Shigu (excluding 1969–1970 and 1988–2006 when data are unavailable). Gray bars indicate the standard deviation of the measured sediment fluxes of $\pm 5.3 \times 10^9$ kg in Batang and $\pm 6.6 \times 10^9$ kg in Shigu, respectively. (b) and (d) Measured sediment flux difference, compared with the linear fit relationship between annual runoff and sediment flux, at the Batang and Shigu hydrological stations. Gray dashed lines indicate the timing of the Baige landslides.

10 km from the river (Figure S5 in Supporting Information S1). Similarly, the first LLOF was not visible at any station (Figure S6 in Supporting Information S1).

To compare the seismic detectability of the catastrophic 2021 Chamoli, India flood (Cook et al., 2021) with our second LLOF, we calculated the average seismic power during the second LLOF and background noise (Cook et al., 2021). We first remove the instrument response and filter at 1–2.5 Hz before calculating the PSD. The 1–2.5 Hz average power during the second LLOF recorded at stations GYXJ (−153.6 dB) and BTA (−152.1 dB) is the mean value of PSD at 19:00–20:00 and 22:30–23: 30 CST on 13 November, respectively. The 1–2.5 Hz background noise PSD recorded at stations GYXJ (−166.0 dB) and BTA (−162.4 dB) is the mean value of PSD at 13:00–14:00 and 20:00–21:00 CST on 13 November, respectively.

The 1–2.5 Hz average power during the catastrophic Chamoli flood was −148.4 dB at station BNG, which was located ~100 km from the river (Cook et al., 2021). This is 3.7 dB higher than the average power during our second LLOF recorded by stations within 10 km of the river, although our LLOF's discharge when passing by stations GYXJ, BAT, CLZJ, and HNXJ (Figure 1c) was >1.5 times than that of the Chamoli flood (Shugar et al., 2021). Furthermore, we find that the background noise levels at stations GYXJ and BTA (<−162.4 dB) were lower than that in the Chamoli region (>−159.1 ± 3.2 dB; Cook et al., 2021). Therefore, the low seismic detectability of our LLOFs compared with the previous study (Cook et al., 2021) is not due to differences in the background noise level and instrument sensitivity.

Furthermore, previous studies assumed that the source of peak seismic energy tracks the point of peak discharge since existing fluid-seismic models (Gimbert et al., 2014; Tsai et al., 2012) predict a power-law relation between discharge and seismic energy. However, our direct in situ discharge measurements show that the peak seismic energy recorded at station BTA preceded the LLOF's peak discharge by ~1.4 hr (Figure 4b).

21699011, 2024, 2, Downloaded from https://agupubs.onlinelibrary.wiley.com/doi/10.1029/2023JF007363 by Université Côte d'Azur, Wiley Online Library on [04/03/2024]. See the Terms and Conditions (https://onlinelibrary.wiley.com/terms-and-conditions) on Wiley Online Library for rules of use; OA articles are governed by the applicable Creative Commons License

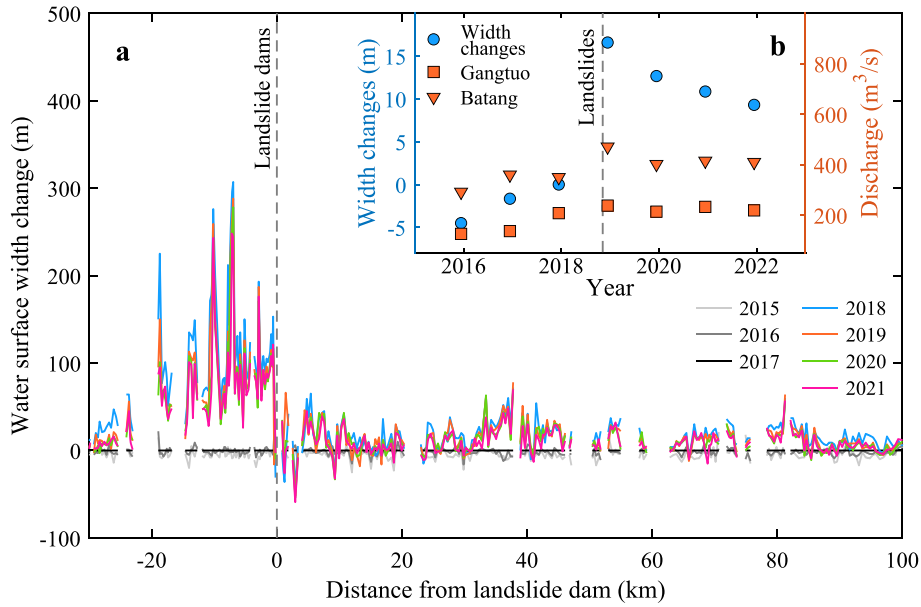

Figure 6. Width changes of the Jinsha River. (a) 2015 to 2021 water surface width changes relative to 2017, from 30 km upstream to 100 km downstream of the landslide dams. Water surface widths are estimated from Sentinel-2 images and have an uncertainty of ±10 m. (b) 2015 to 2021 measured discharge at the Batang (orange triangle) and Gangtuo (orange square) hydrological stations, and average water surface width changes relative to 2017 of the 100 km section downstream from the landslide dams (blue circle).

4.4. Evolution of Sediment Flux and River Width

Historical observations at the Batang and Shigu hydrological stations reveal a linear relationship between annual runoff and sediment flux (Figures 5a and 5c). However, the recorded sediment fluxes at these two stations in 2018 of 4.42×10^{10} and 5.29×10^{10} kg (Figure 5) significantly exceeded the expected sediment fluxes of $1.78 \times 10^{10} \pm 0.53 \times 10^{10}$ and $1.46 \times 10^{10} \pm 0.66 \times 10^{10}$ kg given the runoffs of 3.76×10^{10} and 5.15×10^{10} m^3 respectively (Figure 5). In 2019, the recorded sediment flux in Batang of 2.11×10^{10} kg is similar to the expected sediment flux level while the recorded sediment flux in Shigu of 3.78×10^{10} kg is slightly higher than the expected sediment flux of $2.69 \times 10^{10} \pm 0.66 \times 10^{10}$ kg, given the runoffs of 3.27×10^{10} m^3 and 4.36×10^{10} m^3 respectively which are lower than in 2018 (Figure 5). Interestingly, in 2020 when the annual runoffs increased to 4.12×10^{10} and 5.15×10^{10} m^3, the recorded sediment fluxes of 4.31×10^{10} and 6.28×10^{10} kg at the two stations again significantly exceeded the expected sediment fluxes of $1.25 \times 10^{10} \pm 0.53 \times 10^{10}$ and $2.45 \times 10^{10} \pm 0.66 \times 10^{10}$ kg, respectively (Figure 5). Finally, in 2021, the recorded sediment fluxes at these two stations returned down to the expected levels given the annual runoffs.

Using satellite-based observations (Figure S7 in Supporting Information S1), we also find that after the hazard cascades, the water surface widths of the Jinsha River from 30 km upstream to 100 km downstream of the landslide dams are larger than before the hazard cascades under similar discharge conditions (Figure 6a). Furthermore, while the average water surface width of the 100 km section downstream from the landslide dams remains greater than before the hazard cascades, under similar discharge conditions, this downstream average water surface width has been decreasing continuously from 2018 to 2021 (Figure 6b).

5. Discussion

5.1. Seismic Monitoring and Early Warning of Hazard Cascades

Compared with existing physical models (Gimbert et al., 2014; Tsai et al., 2012) which predict that seismic energy increases with discharge, we find that the second LLOF's peak seismic energy significantly preceded peak discharge (Figures 3 and 4). Although these existing models can explain the seismic energy peak at 18:00 CST on 13 Oct corresponding to the maximum discharge, PSD calculated from the existing models cannot explain our observation of the seismic energy peak that occurred at 16:30 CST on 13 Oct which precedes peak discharge.

21699011, 2024, 2, Downloaded from https://agupubs.onlinelibrary.wiley.com/doi/10.1029/2023JF007363 by Université Côte d'Azur, Wiley Online Library on [04/03/2024]. See the Terms and Conditions (https://onlinelibrary.wiley.com/terms-and-conditions) on Wiley Online Library for rules of use; OA articles are governed by the applicable Creative Commons License

21699011, 2024, 2, Downloaded from https://agupubs.onlinelibrary.wiley.com/doi/10.1029/2023JF007363 by Université Côte d'Azur, Wiley Online Library on [04/03/2024]. See the Terms and Conditions (https://onlinelibrary.wiley.com/terms-and-conditions) on Wiley Online Library for rules of use; OA articles are governed by the applicable Creative Commons License

Furthermore, the second LLOF is relatively quiet compared to a previously recorded LOF with smaller peak discharge (Cook et al., 2021; Maurer et al., 2020). Note that since there are many uncertainties in calculating the propagation media response of high-frequency (>1 Hz) seismic signals for regions where a high-resolution seismic velocity model is not available, and the PSD simulations are in this frequency domain (Gimbert et al., 2014; Tsai et al., 2012), we do not directly calculate the seismic energy radiated by the LLOFs based on these existing models. Nevertheless, it is clear that there exist other physical process(es) that can control the seismic energy radiation during catastrophic flood events. We suggest that channel erodibility and bank slope stability are important controls of seismic energy radiation from LOFs. Before the peak flood discharge, the peak in seismic energy might reflect the channel being significantly eroded which also triggered widespread collapse of the bank slope. Similar channel erosion and bank collapses also occur during dam breaches, and our numerical simulation of the dam breach shows that the peaks of breach expansion and sediment flux preceded peak discharge (Figure 2d). Subsequently, the weaker seismic energy radiated by the flood may be due to the more stable banks of the Jinsha River because the unstable bank slopes had already failed. The channel stability of the Jinsha River near the landslides has been confirmed by many geological surveys (Fan, Lin, et al., 2020; Liu et al., 2017; Zhao et al., 2018), hence ∼10 hydropower stations are being planned/constructed within 20 km upstream and 370 km downstream of the landslides (Wang et al., 2015; Wu et al., 2020). Our conceptual model can explain why during the 1994 Bhutan glacial LOF, only certain river segments radiated detectable seismic energy (Maurer et al., 2020) since they may reflect differences in channel erodibility and/or riverbank stability. This implies that while catastrophic floods along erodible channels with unstable riverbanks might be readily detectable by regional seismic networks, floods along stable channels might be relatively quiet and hence require a denser seismic network to monitor.

While an early warning system for floods using a regional seismic network has been proposed based on the idea that catastrophic floods have been detected ∼100 km away (Cook et al., 2021; Maurer et al., 2020), our observations show that the largest recorded outburst flood in the 21st century to date was undetectable beyond a few kilometers, probably due to variations of river channel stability. Therefore, seismic monitoring and early warning of catastrophic floods need to account for spatiotemporal changes in river channel erodibility, bank stability, and sediment flux-discharge relationship for an accurate estimate of the location, timing, and size of flood events. In comparison, we show that the dam breach processes (slope collapse, turbulent flow, and bedload transport) can be characterized seismically further away and potentially provide warning ∼60 min before discharge exceeds typical monsoon flood levels (Figure 3d). The seismic signals are also more easily distinguishable from other natural and inferred anthropogenic noise sources due to differences in frequency content (Figure 3 and Figure S4 in Supporting Information S1). Thus, seismic monitoring of dam breach can provide earlier and clearer warnings of catastrophic outburst flood events compared to currently proposed early warning systems (Cook et al., 2021; Maurer et al., 2020). These seismic observations can also provide important constraints for numerical modeling of dam breaches.

5.2. Long-Term Impact of Hazard Cascades on River Morphology and Hydrology

Our observations demonstrate that hazard cascades can have a long-term impact on river morphology and hydrology that lasts at least several years. The two Baige landslides transported 3.4×10^7 m^3 of sediments into the Jinsha River. Following the landslide dam breaches, the catastrophic outburst floods not only entrained sediments from the landslide dams but may have also eroded and scraped the river channel, bank, and hillslope (Yang et al., 2021), which resulted in a significant increase in the downstream sediment flux in 2018. As these sediments are transported downstream, some are deposited along the way before being successively re-transferred downstream during the next monsoon seasons, which explains why the recorded sediment fluxes after the hazard cascades are higher than the expected sediment flux level given annual runoff in the following years (Figure 5). On the other hand, the greater water surface width of the 30 km section upstream from the landslide dams (Figure 6a) indicates that the residual dam after the dam breach still blocks the channel, which reduces the flow velocity in this section and thus intercepts some of the incoming sediments (Korup & Montgomery, 2008). A new river knickpoint may thus form here. Therefore, the sediment flux at sections downstream from the landslide dams depends on the relative amount of sediments intercepted by the residual dam and the re-transported sediments that were deposited along the channel during the hazard cascades. If the amount of intercepted sediments is similar to the re-transported sediments, the sediment flux downstream would be similar to the expected sediment flux level given the runoff, as observed at Batang in 2019 (Figure 5a). However, while the amount of intercepted sediments is the same for any site downstream from the landslide dams, more sediments deposited along the river channel after the hazard cascades can be re-transported for sites located farther downstream from the landslide

dams. This could explain why the recorded sediment flux at Shigu in 2019 is higher than the expected sediment flux level given the runoff (Figure 5c). Furthermore, when the annual runoff at the Batang and Shigu hydrological stations in 2020 exceeds that in 2018 and 2019, sediments that were still deposited along the channel due to the hazard cascades were remobilized and thus the recorded sediment fluxes at these two stations in 2020 exceeded the expected sediment flux level given the runoff (Figure 5).

As the sediments deposited along the channel by the hazard cascades were gradually transported further downstream, the amount of sediments that still remained which can be re-transported will decrease over time. This can explain why the sediment fluxes at the Batang and Shigu hydrological stations in 2021 were within the expected sediment flux levels given the annual runoff, though this may also be attributed to the lower annual runoff in 2021 compared to previous years. This is also consistent with our observation that the average water surface width of the 100 km section of Jinsha River downstream from the landslide dams has been decreasing over time, given similar discharge, due to re-transportation of sediments downstream from the landslide dams (Figure 6b). As the downstream sediments deposited along the channel after the hazard cascades are completely transported in the next few years, the interception effect of the residual dam may make the downstream sediment flux lower than the expected sediment flux level given annual runoff, which may benefit the downstream hydropower plants temporarily. However, eventually the residual dam will likely breach completely, at which point the downstream infrastructures will be affected by a significant increase in sediment flux within a short period of time. This increase in sediment flux and its associated organic carbon may change the water quality and affect hundreds of thousands of people and the river ecosystem downstream from the landslide dam.

Assuming a sediment bulk density of 1,300 kg/m^3 (Yang et al., 2014), the increased sediment flux at the Shigu station from 2018 to 2021 due to these hazard cascades is equivalent to a reduction of the storage capacity of the Liyuan hydropower plant ~670 km downstream of the landslide dam (Figure 1a) by $\sim 3.8 \times 10^7 \pm 1.5 \times 10^7$ m^3 which is ~22% ± 9% of the designed regulation storage capacity (1.73×10^8 m^3; Xie et al., 2012). This effect might also be borne by other hydropower plants downstream from the hazard cascades (Figure 1), including three of the four largest existing/planned hydropower plants in the world (Three Gorges, Baihetan, and Xiluodu hydropower plants; Hu et al., 2009). Furthermore, continued hillslope deformation around the Baige landslide scars suggests that more landslides might occur soon (Chen et al., 2021; Fan, Yang, et al., 2020; Zhang, Xiao, et al., 2019) which would further increase the sediment flux. Therefore, catastrophic outburst floods cannot only directly damage/destroy hydropower plants, but the resulting increased sediment fluxes in the years after the hazard cascades can also significantly reduce the designed storage capacity of hydropower plants and reservoirs downstream from the landslide dams, which threatens the region's irrigation capacity and energy security.

6. Conclusion

The hazard cascades initiated by the 2018 Baige landslides in the Tibetan plateau provided a unique opportunity to evaluate our current understanding of seismic monitoring of surface hazards as well as these events' complex dynamics and impact on river systems. Surprisingly, we find that the largest recorded outburst flood in the 21st century to date was seismically undetectable beyond a few kilometers. In addition, contrary to current understanding, the peak seismic energy preceded peak discharge by hours. Therefore, we suggest that accurate seismic monitoring of catastrophic floods requires accounting for spatiotemporal changes in the sediment flux-discharge relationship. In addition, seismic monitoring of dam breaches may provide some of the earliest warnings of potential outburst floods as well as important constraints on dam breach evolution. Finally, our observations demonstrate that such hazard cascades can drastically change the geomorphology and hydrology of river systems up to at least 670 km downstream for at least a few years. Accordingly, the increased sediment fluxes in the years following the hazard cascades may have significantly reduced the storage capacity of a hydropower plant 670 km downstream. Therefore, our results highlight the need to consider the long-term effects of surface hazards on river systems during hydropower plant and land use planning.

21699011, 2024, 2, Downloaded from https://agupubs.onlinelibrary.wiley.com/doi/10.1029/2023JF007363 by Université Côte d'Azur, Wiley Online Library on [04/03/2024]. See the Terms and Conditions (https://onlinelibrary.wiley.com/terms-and-conditions) on Wiley Online Library for rules of use; OA articles are governed by the applicable Creative Commons License

Data Availability Statement

The software DLBreach used in this study are publicly available at https://webspace.clarkson.edu/~wwu/DLBreach.html. The Sentinel-2 data are available at https://www.sentinel-hub.com. Hydrological data are available at Zhang et al. (2023) https://doi.org/10.5281/zenodo.7849298. Waveform data used in this study are provided by the Sichuan Earthquake Administration and are available at Zhang and Su. (2023) https://doi.org/10.5281/zenodo.8147072. DEM data are provided by ASTER (https://asterweb.jpl.nasa.gov).

Acknowledgments
We thank Associate Editor Matthew J. Brain, Luobin Yan and two anonymous reviewers for their thoughtful reviews of the manuscript. We thank L. L. Zhu for valuable discussions and the Changjiang Water Resources Commission for providing the gauge data. This work was supported by the Croucher Tak Wah Mak Innovation Award, CUHK Direct Grant for Research (Grant 4053594), CUHK Research Fellowship Scheme (Grant 4200720), CUHK Postdoctoral Fellowship Scheme (Grant 3135043), the National Key Research and Development program of China (Grant 2022YFF0800604), and the Major Program of the National Natural Science Foundation of China (Grant 42090051). The salary of M. Chmiel was paid by the WSL program Climate Change Impacts on Alpine Mass Movements (CCAMM) and Observatoire de la Côte d'Azur Henri Poincaré Postdoctoral fellowship.

References

Anees, M. T., Abdullah, K., Nawawi, M., Ab Rahman, N. N. N., Piah, A. R. M., Zakaria, N. A., et al. (2016). Numerical modeling techniques for flood analysis. *Journal of African Earth Sciences*, *124*, 478–486. https://doi.org/10.1016/j.jafrearsci.2016.10.001

Arattano, M., & Marchi, L. (2008). Systems and sensors for debris-flow monitoring and warning. *Sensors*, *8*(4), 2436–2452. https://doi.org/10.3390/s8042436

Armanini, A., & Di Silvio, G. (1988). A one-dimensional model for the transport of a sediment mixture in non-equilibrium conditions. *Journal of Hydraulic Research*, *26*(3), 275–292. https://doi.org/10.1080/00221688809499212

Bakker, M., Gimbert, F., Geay, T., Misset, C., Zanker, S., & Recking, A. (2020). Field application and validation of a seismic bedload transport model. *Journal of Geophysical Research: Earth Surface*, *125*(5), e2019JF005416. https://doi.org/10.1029/2019jf005416

Chen, F., Gao, Y., Zhao, S., Deng, J., Li, Z., Ba, R., et al. (2021). Kinematic process and mechanism of the two slope failures at Baige Village in the upper reaches of the Jinsha River, China. *Bulletin of Engineering Geology and the Environment*, *80*(4), 3475–3493. https://doi.org/10.1007/s10064-021-02146-0

Chen, Z., Chen, S., Wang, L., Zhong, Q., Zhang, Q., & Jin, S. (2020). Back analysis of the breach flood of the "11.03" Baige barrier lake at the Upper Jinsha River. *Scientia Sinica Technologica*, *50*(6), 763–774. https://doi.org/10.1360/SST-2019-0297

Chmiel, M., Godano, M., Piantini, M., Brigode, P., Gimbert, F., Bakker, M., et al. (2022). Brief communication: Seismological analysis of flood dynamics and hydrologically triggered earthquake swarms associated with Storm Alex. *Natural Hazards and Earth System Sciences*, *22*(5), 1541–1558. https://doi.org/10.5194/nhess-22-1541-2022

Cook, K. L., Andermann, C., Gimbert, F., Adhikari, B. R., & Hovius, N. (2018). Glacial lake outburst floods as drivers of fluvial erosion in the Himalaya. *Science*, *362*(6410), 53–57. https://doi.org/10.1126/science.aat4981

Cook, K. L., Rekapalli, R., Dietze, M., Pilz, M., Cesca, S., Rao, N. P., et al. (2021). Detection and potential early warning of catastrophic flow events with regional seismic networks. *Science*, *374*(6563), 87–92. https://doi.org/10.1126/science.abj1227

Delaney, K. B., & Evans, S. G. (2015). The 2000 Yigong landslide (Tibetan Plateau), rockslide-dammed lake and outburst flood: Review, remote sensing analysis, and process modelling. *Geomorphology*, *246*, 377–393. https://doi.org/10.1016/j.geomorph.2015.06.020

Dietze, M., Hoffmann, T., Bell, R., Schrott, L., & Hovius, N. (2022). A seismic approach to flood detection and characterization in upland catchments. *Geophysical Research Letters*, *49*(20), e2022GL100170. https://doi.org/10.1029/2022gl100170

Ekström, G., & Stark, C. P. (2013). Simple scaling of catastrophic landslide dynamics. *Science*, *339*(6126), 1416–1419. https://doi.org/10.1126/science.1232887

Fan, Q., Lin, P., Jiang, S., Wei, P., & Li, G. (2020). Review on the rock mechanics and engineering practice for large hydropower stations along the downstream section of the Jinsha River. *Journal of Tsinghua University*, *60*(7), 537–556.

Fan, X., Yang, F., Siva Subramanian, S., Xu, Q., Feng, Z., Mavrouli, O., et al. (2020). Prediction of a multi-hazard chain by an integrated numerical simulation approach: The Baige landslide, Jinsha River, China. *Landslides*, *17*(1), 147–164. https://doi.org/10.1007/s10346-019-01313-5

Feng, Z. (2009). The seismic signatures of the surge wave from the 2009 Xiaolin landslide-dam breach in Taiwan. *Hydrological Processes*, *26*(9), 1342–1351. https://doi.org/10.1002/hyp.8239

Gao, Y., Zhao, S., Deng, J., Yu, Z., & Rahman, M. (2021). Flood assessment and early warning of the reoccurrence of river blockage at the Baige landslide. *Journal of Geographical Sciences*, *31*(11), 1694–1712. https://doi.org/10.1007/s11442-021-1918-9

Garcia-Castellanos, D., & O'Connor, J. E. (2018). Outburst floods provide erodability estimates consistent with long-term landscape evolution. *Scientific Reports*, *8*(1), 10573. https://doi.org/10.1038/s41598-018-28981-y

Gariano, S. L., & Guzzetti, F. (2016). Landslides in a changing climate. *Earth-Science Reviews*, *162*, 227–252. https://doi.org/10.1016/j.earscirev.2016.08.011

Gimbert, F., Tsai, V. C., & Lamb, M. P. (2014). A physical model for seismic noise generation by turbulent flow in rivers. *Journal of Geophysical Research: Earth Surface*, *119*(10), 2209–2238. https://doi.org/10.1002/2014jf003201

Habersack, H., Kreisler, A., Rindler, R., Aigner, J., Seitz, H., Liedermann, M., & Laronne, J. B. (2017). Integrated automatic and continuous bedload monitoring in gravel bed rivers. *Geomorphology*, *29*, 80–93. https://doi.org/10.1016/j.geomorph.2016.10.020

Hewawasam, T. (2010). Effect of land use in the upper Mahaweli catchment area on erosion, landslides and siltation in hydropower reservoirs of Sri Lanka. *Journal of the National Science Foundation of Sri Lanka*, *38*(1), 3–14. https://doi.org/10.4038/jnsfsr.v38i1.1721

Hovius, N., Stark, C. P., & Allen, P. A. (1997). Sediment flux from a mountain belt derived by landslide mapping. *Geology*, *25*(3), 231–234. https://doi.org/10.1130/0091-7613(1997)025<0231:sffamb>2.3.co;2

Hu, B., Yang, Z., Wang, H., Sun, X., Bi, N., & Li, G. (2009). Sedimentation in the Three Gorges Dam and the future trend of Changjiang (Yangtze River) sediment flux to the sea. *Hydrology and Earth System Sciences*, *13*(11), 2253–2264. https://doi.org/10.5194/hess-13-2253-2009

Irons, J. R., Dwyer, J. L., & Barsi, J. A. (2012). The next Landsat satellite: The Landsat data continuity mission. *Remote Sensing of Environment*, *122*, 11–21. https://doi.org/10.1016/j.rse.2011.08.026

Iverson, R. M., Reid, M. E., Logan, M., LaHusen, R. G., Godt, J. W., & Griswold, J. P. (2011). Positive feedback and momentum growth during debris-flow entrainment of wet bed sediment. *Nature Geoscience*, *4*(2), 116–121. https://doi.org/10.1038/ngeo1040

Jaedicke, C., Solheim, A., Blikra, L., Stalsberg, K., Sorteberg, A., Aaheim, A., et al. (2008). Spatial and temporal variations of Norwegian geohazards in a changing climate, the GeoExtreme Project. *Natural Hazards and Earth System Sciences*, *8*(4), 893–904. https://doi.org/10.5194/nhess-8-893-2008

Khrapov, S. S., Pisarev, A. V., Kobelev, I. A., Zhumaliev, A. G., Agafonnikova, E. O., Losev, A. G., & Khoperskov, A. V. (2013). The numerical simulation of shallow water: Estimation of the roughness coefficient on the flood stage. *Advances in Mechanical Engineering*, *5*, 787016. https://doi.org/10.1155/2013/787016

Korup, O., & Montgomery, D. R. (2008). Tibetan plateau river incision inhibited by glacial stabilization of the Tsangpo gorge. *Nature*, *455*(7214), 786–789. https://doi.org/10.1038/nature07322

21699011, 2024, 2, Downloaded from https://agupubs.onlinelibrary.wiley.com/doi/10.1029/2023JF007363 by Université Côte d'Azur, Wiley Online Library on [04/03/2024]. See the Terms and Conditions (https://onlinelibrary.wiley.com/terms-and-conditions) on Wiley Online Library for rules of use; OA articles are governed by the applicable Creative Commons License

Le Guern, J., Rodrigues, S., Geay, T., Zanker, S., Hauet, A., Tassi, P., et al. (2020). Relevance of acoustic methods to quantify bedload transport and bedform dynamics in large sandy-gravel bed river. *Earth Surface Dynamics*, *9*(3), 423–444. https://doi.org/10.5194/esurf-9-423-2021

Liu, L., Zhao, Q., & Han, G. (2017). Characteristics of deep-seated crack in dam site of Yebatan Hydropower Station. *Chinese Journal of Geotechnical Engineering*, *39*, 501–508.

Maurer, J., Schaefer, J., Russell, J., Rupper, S., Wangdi, N., Putnam, A., & Young, N. (2020). Seismic observations, numerical modeling, and geomorphic analysis of a glacier lake outburst flood in the Himalayas. *Science Advances*, *6*(38), eaba3645. https://doi.org/10.1126/sciadv.aba3645

McArdell, B. W., Bartelt, P., & Kowalski, J. (2007). Field observations of basal forces and fluid pore pressure in a debris flow. *Geophysical Research Letters*, *34*(7), L07406. https://doi.org/10.1029/2006gl029183

McCoy, S. W., Kean, J. W., Coe, J. A., Staley, D. M., Wasklewicz, T. A., & Tucker, G. E. (2010). Evolution of a natural debris flow: In situ measurements of flow dynamics, video imagery, and terrestrial laser scanning. *Geology*, *38*(8), 735–738. https://doi.org/10.1130/g30928.1

NDRCC. (2018a). *Basic situation of natural disasters in China in November 2018*. National Disaster Reduction Center of China (NDRCC). Retrieved from https://www.ndrcc.org.cn/zqtj/6097.jhtml

NDRCC. (2018b). *Basic situation of natural disasters in China in October 2018*. National Disaster Reduction Center of China (NDRCC). Retrieved from https://www.ndrcc.org.cn/zqtj/5367.jhtml

Ozturk, U., Bozzolan, E., Holcombe, E. A., Shukla, R., Pianosi, F., & Wagener, T. (2022). How climate change and unplanned urban sprawl bring more landslides. *Nature*, *608*(7922), 262–265. https://doi.org/10.1038/d41586-022-02141-9

Price, M. F. (2013). *Mountain geography: Physical and human dimensions*. University of California Press.

Sánchez, A., & Wu, W. (2011). A non-equilibrium sediment transport model for coastal inlets and navigation channels. *Journal of Coastal Research*, *59*(59), 39–48. https://doi.org/10.2112/si59-005.1

Schaller, M., von Blanckenburg, F., Hovius, N., & Kubik, P. W. (2001). Large-scale erosion rates from in situ-produced cosmogenic nuclides in European river sediments. *Earth and Planetary Science Letters*, *188*(3–4), 441–458. https://doi.org/10.1016/s0012-821x(01)00320-x

Schweizer, J., Bruce Jamieson, J., & Schneebeli, M. (2003). Snow avalanche formation. *Reviews of Geophysics*, *41*(4), 1016. https://doi.org/10.1029/2002rg000123

Shang, Y., Yang, Z., Li, L., Liao, Q., & Wang, Y. (2003). A super-large landslide in Tibet in 2000: Background, occurrence, disaster, and origin. *Geomorphology*, *54*(3–4), 225–243. https://doi.org/10.1016/s0169-555x(02)00358-6

Shugar, D. H., Jacquemart, M., Shean, D., Bhushan, S., Upadhyay, K., Sattar, A., et al. (2021). A massive rock and ice avalanche caused the 2021 disaster at Chamoli, Indian Himalaya. *Science*, *373*(6552), 300–306. https://doi.org/10.1126/science.abh4455

Singh, K. P., & Snorrason, A. (1984). Sensitivity of outflow peaks and flood stages to the selection of dam breach parameters and simulation models. *Journal of Hydrology*, *68*(1–4), 295–310. https://doi.org/10.1016/0022-1694(84)90217-8

Tralli, D. M., Blom, R. G., Zlotnicki, V., Donnellan, A., & Evans, D. L. (2005). Satellite remote sensing of earthquake, volcano, flood, landslide and coastal inundation hazards. *ISPRS Journal of Photogrammetry and Remote Sensing*, *59*(4), 185–198. https://doi.org/10.1016/j.isprsjprs.2005.02.002

Tramblay, Y., Villarini, G., & Zhang, W. (2020). Observed changes in flood hazard in Africa. *Environmental Research Letters*, *15*(10), 1040b5. https://doi.org/10.1088/1748-9326/abb90b

Tsai, V. C., Minchew, B., Lamb, M. P., & Ampuero, J. P. (2012). A physical model for seismic noise generation from sediment transport in rivers. *Geophysical Research Letters*, *39*(2). https://doi.org/10.1029/2011gl050255

Vericat, D., Church, M., & Batalla, R. J. (2006). Bed load bias: Comparison of measurements obtained using two (76 and 152 mm) Helley-Smith samplers in a gravel bed river. *Water Resources Research*, *42*(1), W01402. https://doi.org/10.1029/2005wr004025

Wahl, T. L. (2004). Uncertainty of predictions of embankment dam breach parameters. *Journal of Hydraulic Engineering*, *130*(5), 389–397. https://doi.org/10.1061/(asce)0733-9429(2004)130:5(389)

Wang, C., Zhou, J., Lu, P., & Yuan, L. (2015). Long-term scheduling of large cascade hydropower stations in Jinsha River, China. *Energy Conversion and Management*, *90*, 476–487. https://doi.org/10.1016/j.enconman.2014.11.024

Wang, R. (1999). A simple orthonormalization method for stable and efficient computation of Green's functions. *Bulletin of the Seismological Society of America*, *89*(3), 733–741. https://doi.org/10.1785/bssa0890030733

Wang, Z., & Bowles, D. S. (2006). Three-dimensional non-cohesive earthen dam breach model. Part 1: Theory and methodology. *Advances in Water Resources*, *29*(10), 1528–1545. https://doi.org/10.1016/j.advwatres.2005.11.009

Wasowski, J., & Bovenga, F. (2014). Investigating landslides and unstable slopes with satellite Multi Temporal Interferometry: Current issues and future perspectives. *Engineering Geology*, *174*, 103–138. https://doi.org/10.1016/j.enggeo.2014.03.003

Wu, W. (2013). Simplified physically based model of earthen embankment breaching. *Journal of Hydraulic Engineering*, *139*(8), 837–851. https://doi.org/10.1061/(asce)hy.1943-7900.0000741

Wu, W. (2016). *Introduction to DLBreach–A simplified physically-based dam/Levee breach model*. Clarkson University.

Wu, Y., Fang, H., Huang, L., & Ouyang, W. (2020). Changing runoff due to temperature and precipitation variations in the dammed Jinsha River. *Journal of Hydrology*, *582*, 124500. https://doi.org/10.1016/j.jhydrol.2019.124500

Xie, W., Ji, C. M., Yang, Z. J., & Zhang, X. X. (2012). Short-term power generation scheduling rules for cascade hydropower stations based on hybrid algorithm. *Water Science and Engineering*, *5*, 46–58.

Yang, C. M., Chang, J. M., Hung, C. Y., Lu, C. H., Chao, W. A., & Kang, K. H. (2022). Life span of a landslide dam on mountain valley caught on seismic signals and its possible early warnings. *Landslides*, *19*(3), 637–646. https://doi.org/10.1007/s10346-021-01818-y

Yang, S. L., Milliman, J. D., Xu, K. H., Deng, B., Zhang, X. Y., & Luo, X. X. (2014). Downstream sedimentary and geomorphic impacts of the Three Gorges Dam on the Yangtze River. *Earth-Science Reviews*, *138*, 469–486. https://doi.org/10.1016/j.earscirev.2014.07.006

Yang, W., Fang, J., & Liu-Zeng, J. (2021). Landslide-lake outburst floods accelerate downstream hillslope slippage. *Earth Surface Dynamics*, *9*(5), 1251–1262. https://doi.org/10.5194/esurf-9-1251-2021

Yavari-Ramshe, S., & Ataie-Ashtiani, B. (2016). Numerical modeling of subaerial and submarine landslide-generated tsunami waves—Recent advances and future challenges. *Landslides*, *13*(6), 1325–1368. https://doi.org/10.1007/s10346-016-0734-2

Zhang, L., Xiao, T., He, J., & Chen, C. (2019). Erosion-based analysis of breaching of Baige landslide dams on the Jinsha River, China, in 2018. *Landslides*, *16*(10), 1965–1979. https://doi.org/10.1007/s10346-019-01247-y

Zhang, S., Xie, X., Wei, F., Chernomorets, S., Petrakov, D., Pavlova, I., & Tellez, R. D. (2015). A seismically triggered landslide dam in Honshiyan, Yunnan, China: From emergency management to hydropower potential. *Landslides*, *12*(6), 1147–1157. https://doi.org/10.1007/s10346-015-0639-5

Zhang, Z., He, S., Liu, W., Liang, H., Yan, S., Deng, Y., et al. (2019). Source characteristics and dynamics of the October 2018 Baige landslide revealed by broadband seismograms. *Landslides*, *16*(4), 777–785. https://doi.org/10.1007/s10346-019-01145-3

Zhang, Z., & Su, J. (2023). The waveform data for the 2018 Baige hazard cascades. *Zenodo*. https://doi.org/10.5281/zenodo.8147072

21699011, 2024, 2, Downloaded from https://agupubs.onlinelibrary.wiley.com/doi/10.1029/2023JF007363 by Université Côte d'Azur, Wiley Online Library on [04/03/2024]. See the Terms and Conditions (https://onlinelibrary.wiley.com/terms-and-conditions) on Wiley Online Library for rules of use; OA articles are governed by the applicable Creative Commons License

Zhang, Z., Tan, Y. J., W, F., He, S., & Chmiel, M. (2023). Measured data of 2018 Baige lake-dammed lake outburst floods. *Zenodo*. https://doi.org/10.5281/zenodo.7849298

Zhang, Z., Walter, F., McArdell, B. W., Wenner, M., Chmiel, M., de Haas, T., & He, S. (2021). Insights from the particle impact model into the high-frequency seismic signature of debris flows. *Geophysical Research Letters*, *48*(1), e2020GL088994. https://doi.org/10.1029/2020gl088994

Zhao, C., Kang, Y., Zhang, Q., Lu, Z., & Li, B. (2018). Landslide identification and monitoring along the Jinsha River catchment (Wudongde reservoir area), China, using the InSAR method. *Remote Sensing*, *10*(7), 993. https://doi.org/10.3390/rs10070993

Zhong, Q., Chen, S., Wang, L., & Shan, Y. (2020). Back analysis of breaching process of Baige landslide dam. *Landslides*, *17*(7), 1681–1692. https://doi.org/10.1007/s10346-020-01398-3

21699011, 2024, 2, Downloaded from https://agupubs.onlinelibrary.wiley.com/doi/10.1029/2023JF007363 by Université Côte d'Azur, Wiley Online Library on [04/03/2024]. See the Terms and Conditions (https://onlinelibrary.wiley.com/terms-and-conditions) on Wiley Online Library for rules of use; OA articles are governed by the applicable Creative Commons License